fluids

MDPI

Article

Effects of Variable-Speed Operation on the External Characteristics and Work Performance of Multiphase Pumps

Rui Guo [1], Guangtai Shi [2,*], Zhongbin Chen [1], Qingxi Pei [1], Tongde Feng [1] and Aijing Deng [2]

[1] Changqing Oilfield No. 7 Oil Production Plant, Standardization, Xi'an 710200, China; 18608396853@163.com (R.G.); 18008077064@163.com (Z.C.); 18764750500@163.com (Q.P.); 15390292186@163.com (T.F.)

[2] Key Laboratory of Fluid and Power Machinery, Ministry of Education, Xihua University, Chengdu 610039, China; ajok24@126.com

* Correspondence: sgtaixh@126.com

Abstract

Multiphase pumps are key equipment for the efficient transport of multiphase fluids in the petroleum industry, and their transient stability under variable-speed conditions directly affects system reliability. By combining numerical simulation with experimental validation, this study systematically investigates the evolution of external characteristics, energy conversion mechanisms, and the dynamic response of the internal flow field during a 0.4 s variable-frequency speed regulation cycle at inlet gas volume fractions (IGVFs) of 10% and 20%. The numerical model was validated against experimental measurements of a four-stage multiphase pump under pure-water steady-state conditions, with deviations in head, efficiency, and power all within 5%. The results show that during acceleration, the increase in hydraulic efficiency at the lower IGVF is greater than that at the higher IGVF; once deceleration begins, IGVF has no significant effect on hydraulic efficiency. At the investigated IGVFs of 10% and 20%, a higher IGVF increases the transient sensitivity of the internal flow field to speed variation, and increasing IGVF suppresses energy conversion in the impeller. The principal novelty of this work lies in the temporal decomposition of impeller work into dynamic and static pressure components during transient speed variation, revealing that static pressure power consistently accounts for more than 50% of the total power throughout the speed regulation cycle. As rotational speed increases, dynamic pressure power rises because the circumferential velocity of the fluid increases with impeller peripheral speed, while static pressure power also increases continuously owing to the enhanced static pressure work of the blades. During deceleration, the impeller's energy transfer capability weakens with decreasing rotational speed, and both dynamic and static pressure power decline. These findings elucidate the coupled evolution of gas–liquid two-phase flow under variable-speed conditions and provide a theoretical basis for the operational optimization and speed control of multiphase pumps.

Keywords: multiphase pump; variable speed; inlet gas volume fraction; external characteristics; work performance

Check for updates

Academic Editors: Tomoaki Kunugi, Maosen Xu, Huaiyu Cheng and Shun Xu

Received: 25 July 2026
Revised: 9 September 2026
Accepted: 9 September 2026
Published: 11 September 2026

Copyright: © 2026 by the authors. Licensee MDPI, Basel, Switzerland. This article is an open access article distributed under the terms and conditions of the Creative Commons Attribution (CC BY) license.

1. Introduction

Compared with conventional centrifugal or screw pump transport systems, multiphase transport technology can substantially simplify pipeline systems and reduce infrastructure investment, and has therefore become a major focus of industrial research [1]. In practice, however, multiphase pumps frequently operate under off-design conditions, resulting in

low efficiency and increased energy consumption. Variable-frequency speed regulation is commonly used to accommodate fluctuations in incoming flow and ensure uninterrupted oil and gas transport, but the internal flow instability induced by speed variation requires further investigation.

Against this background, extensive research has been conducted on the internal flow field and variable-speed characteristics of multiphase pumps. Minemura and Murakami [1,2] were the first to relate centrifugal pump performance to the gas–liquid two-phase flow patterns within the impeller, laying the foundation for flow visualization and modeling. Using high-speed photography and numerical simulation, Zhang et al. [3] found that gas pocket flow readily develops in the passages as IGVF increases. Yu et al. [4] further demonstrated that the locations of gas-phase meridional vortices closely coincide with gas accumulation regions. Using an Eulerian–Eulerian model, Deng et al. [5] showed that increasing tip clearance intensifies leakage flow and makes the gas volume fraction distribution within the impeller more uniform but reduces efficiency.

With respect to variable-speed operation, Yu et al. [6] combined entropy production theory with flow field analysis and found that energy loss and shear stress increase markedly with inlet velocity. Turbulent entropy production was substantially greater than direct entropy production, and the velocity gradient played a decisive role in entropy production loss and shear stress. Lu et al. [7] regulated the variable-speed operation of a pump turbine using a dynamic speed control model based on Bayesian functions and analyzed the associated energy losses using entropy production theory. Pressure pulsation is a key indicator of pump operating stability. Tsukamoto and Ohashi [8] investigated centrifugal pump acceleration during startup theoretically and experimentally and showed that pulsating pressure around the blades causes the transient startup characteristics to differ markedly from the corresponding quasi-steady behavior. Tan et al. [9] studied a single-blade centrifugal pump and found that reducing rotational speed decreases pressure pulsation intensity.

Under variable-speed conditions, pressure pulsation is closely associated with vortex evolution. Yu et al. [10] analyzed the relationship between vortex rope evolution and low-frequency pressure pulsation in a pump turbine under off-design conditions. Their results showed that a vortex rope generally forms in the guide vane passages during off-design operation and induces low-frequency pressure pulsations. Luo et al. [11] reported that, at different flow rates, the amplitude of rotational-speed fluctuations at cavitation inception is significantly greater than that under severe cavitation or non-cavitating conditions. By comparing three speed regulation modes with constant, increasing, and decreasing acceleration, Zuo et al. [12] found that gradually decreasing acceleration provides the smoothest operation at high rotational speeds and during the transition to steady state.

In offshore oil and gas development, multiphase pumps are core equipment for the efficient transport of gas–liquid two-phase mixtures. At high gas volume fractions (GVF $\geq$50%), however, gas accumulation causes flow field asymmetry, aggravated energy loss, and abrupt head degradation, severely limiting pump reliability and applicability [13,14]. Through experiments and numerical simulations, Li et al. [14] found that as IGVF increased from 0% to 25%, the head and efficiency of a multistage multiphase pump decreased nonlinearly because of intensified gas–liquid separation within the impeller and a reduction in the effective flow area of the passages. Xu et al. [15] measured transient pressure in a helico-axial multiphase pump and found that, under high-flow-rate conditions, the high-speed liquid flow at the impeller outlet intensified turbulent gas–liquid mixing and markedly increased the amplitude at the dominant pressure pulsation frequency. Under low-flow-rate conditions, local backflow is more likely to occur, further reducing energy conversion efficiency. Based on entropy production theory, Ji et al. [16] found that turbulent

dissipation is the principal cause of efficiency loss at large tip clearance, whereas viscous friction dominates at small tip clearance.

Although entropy production analysis has been widely used to quantify energy losses in fluid machinery under steady-state and variable-speed conditions [6,7,16], direct comparisons between entropy production-based loss characterization and the dynamic/static power decomposition approach employed in the present study remain limited. The present work complements these entropy-based investigations by providing a temporal decomposition of impeller work into dynamic and static pressure components during transient speed variation, offering a complementary perspective on energy conversion mechanisms that is distinct from entropy production loss analysis.

Vortex identification methods have continued to evolve in recent years. Liu et al. [17] proposed the Rortex method and provided a detailed mathematical interpretation of, and relationship between, the Q criterion and ΩR. Taking an axial-flow pump as the research object, Ref. [18] compared the Q-criterion and Liutex methods for identifying inlet vortices and examined interactions between the vortices and the impeller. Nayak et al. [19] and Wu et al. [20] clarified the physical basis of unstable flow and discussed the velocity field theory of fluid elements in detail. Using the Ω vortex criterion, Zhang et al. [21] confirmed that internal vortices are a key factor inducing pump-turbine instability. Han [22] used the same criterion to show that, as the cavitation number decreases in a waterjet propulsion pump, the number of vortex structures in the passage increases and the pump's flow-handling capacity decreases. Xie [23] compared several vortex identification methods for a mixed-flow pump and found that the Q criterion provided the clearest identification; vortical structures such as blade-edge separation vortices and trailing-edge separation vortices readily formed in the impeller. Feng et al. [24] found that vortices in the tip clearance region of an axial-flow pump increase the pressure pulsation amplitude along the blade from hub to shroud.

Considerable research has been conducted on the variable-speed characteristics and internal vortex evolution of fluid machinery, and substantial progress has been achieved. Nevertheless, the transient evolution of pressure distribution and energy conversion mechanisms in multiphase pumps under programmed variable-speed conditions—particularly the coupled effects of rotational-speed variation and inlet gas volume fraction—remain insufficiently understood. This study therefore focuses on the effects of rotational-speed variation on internal flow stability and work performance during variable-speed operation, with the aim of providing a theoretical basis for improving the operating stability and speed regulation performance of multiphase pumps.

2. Principle of Variable-Frequency Regulation for the Multiphase Pump

To investigate the variable-speed operating characteristics of multiphase pumps, numerical simulations were performed, with particular emphasis on transient flow instability. Figure 1 presents the measured rotational speed history during variable-frequency speed regulation. The total simulated duration was 0.4 s. The pump first operated steadily at the rated speed for 0.25 s and then entered a 0.15 s variable-speed stage, during which the rotational speed first increased and then decreased. Six representative instants were selected for detailed flow field analysis: t = 0.25 s (initial steady state), 0.27 s (early acceleration), 0.30 s (peak speed), 0.33 s (early deceleration), 0.35 s (mid-deceleration), and 0.40 s (end of deceleration), as marked in Figure 1. By dynamically controlling impeller speed, the transient physical characteristics of the pump throughout the acceleration and deceleration processes were systematically analyzed.

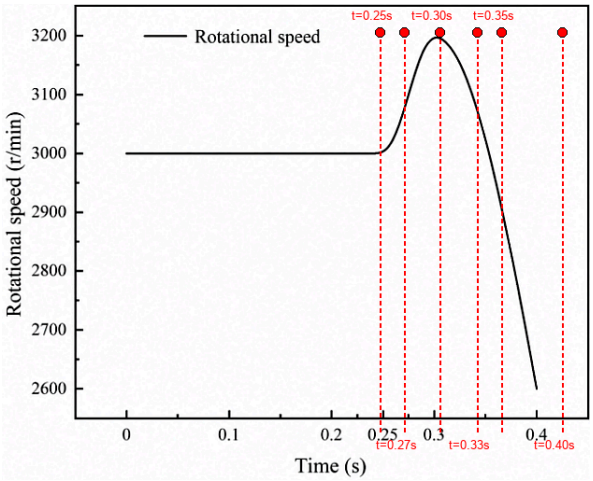


Figure 1. Speed variation of multiphase pumps during variable–frequency speed control.

The six marked instants (t = 0.25, 0.27, 0.30, 0.33, 0.35, and 0.40 s) correspond to the flow field analysis time points. The rotational-speed profile is expressed by Equation (1):

$$n = \begin{cases} 3000 & \mathrm{t} \leq 0.25\mathrm{s} \\ 100\sin(20\pi t + \pi/2) + 3100 & 0.25\mathrm{s} < \mathrm{t} \leq 0.3\mathrm{s} \\ 600\sin(5\pi t + \pi) + 2600 & 0.3\mathrm{s} < t \leq 0.4\mathrm{s} \end{cases} \quad (1)$$

3. Numerical Setup

3.1. Physical Model

The research object was a single-stage multiphase pump. Its overall geometry and flow-through components are shown in Figure 2. The model comprised four principal domains: an inlet extension, a helico-axial impeller, a diffuser, and an outlet extension. The principal geometric and design performance parameters are listed in Table 1.

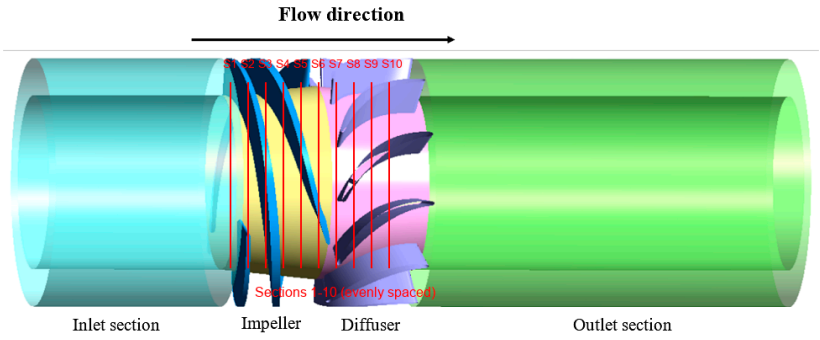


Figure 2. Geometric model of single–stage multiphase pump.

Table 1. Design parameters of multiphase pump.

Parameter/Symbol (Unit)	Value
Design flow rate, Q (m^3/h)	200
Design rotational speed, n (r/min)	3000
Numbers of impeller/diffuser blades, Z_i/Z_d	3 & 11
Impeller/diffuser outer diameters, D_i/D_d (mm)	234
Impeller/diffuser axial lengths, e_i/e_d (mm)	90 & 95

3.2. Grid of Computational Domain

The computational domain consisted of the inlet and outlet extensions, impeller, and diffuser. To ensure reliable simulation results, fully hexahedral structured meshes were

generated throughout the domain. ICEM CFD 2022 R2 (ANSYS Inc., Pittsburgh, PA, USA) was used to mesh the axisymmetric inlet and outlet extensions, while TurboGrid 2022 R2 (ANSYS Inc., Pittsburgh, PA, USA) was used for the geometrically complex impeller and diffuser domains. O-grid topology and local refinement were applied at the blade roots, in regions of high curvature, and near walls to control mesh quality and improve numerical accuracy. The impeller and diffuser meshes are shown in Figure 3.

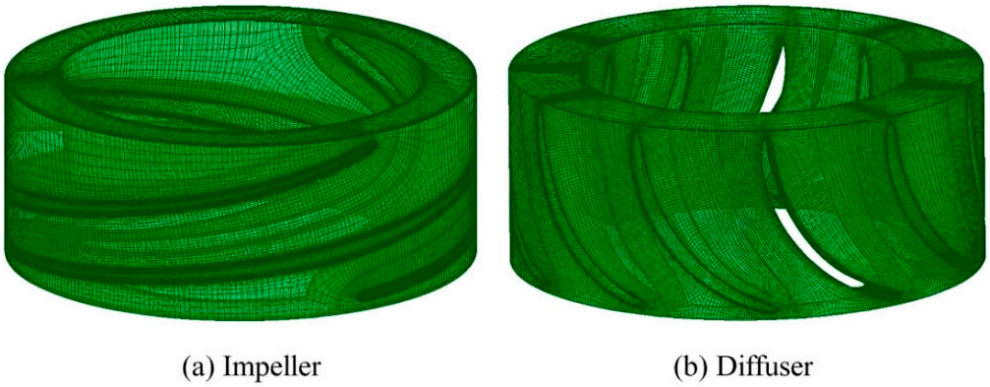


Figure 3. Grid of computational domain.

3.3. Independence of Mesh Density

High-quality meshing is a prerequisite for accurate numerical simulation, and a reliable numerical solution requires an appropriate mesh size. Mesh independence was assessed under pure-water conditions using four mesh schemes. Hydraulic efficiency and head were calculated using Equations (2) and (3), respectively:

$$\eta = \frac{\rho g Q H}{M\omega} \tag{2}$$

$$H = \frac{(P_{\text{out}} - P_{in})}{\rho g} \tag{3}$$

For the two-phase variable-speed simulations, the hydraulic efficiency is defined as $\eta = (\rho \text{m} \cdot \text{g} \cdot Q\text{m} \cdot H)/(\text{M}\omega)$, where ρm is the volume-weighted mixture density at the inlet, Qm is the inlet mixture volume flow rate, H is the total head derived from the total pressure rise across the pump, and M and ω are the instantaneous shaft torque and rotational speed, respectively. Gas compressibility is accounted for through the ideal gas law applied to the dispersed phase. Note that the head in Equation (3) refers to the static pressure rise, while the efficiency calculation uses the total head, including the dynamic component.

As shown in Table 2, the deviations in head and efficiency from the finest mesh (mesh Scheme 4, 612 × 104 elements) decreased as the mesh size increased. Beyond mesh Scheme 3, the head and efficiency deviations from the finest mesh were 0.85% and 1.15%, respectively, both parameters became essentially stable and the numerical error remained within an acceptable range. Considering both computational cost and solution accuracy, mesh Scheme 3 was selected for the subsequent simulations.

Table 2. Independence of mesh density.

Scheme	Mesh Count (104)	Head Deviation from Finest Mesh (%)	Efficiency Deviation from Finest Mesh (%)
1	240	5.93	3.94
2	380	3.76	2.11
3	503	0.85	1.15
4	612	0.00 (ref.)	0.00 (ref.)

3.4. Boundary Conditions

The working medium was an air–water two-phase mixture. Pure water was specified as the continuous liquid phase, and air at 25 °C was specified as the dispersed gas phase with a bubble diameter of 0.1 mm. The SST k-ω turbulence model was used for the liquid phase, and the Dispersed Phase Zero Equation model was used for the gas phase. The Dispersed Phase Zero Equation model was selected because the gas phase remains uniformly dispersed as small bubbles (0.1 mm) at the moderate IGVFs (10–20%) investigated in this study, and the turbulent viscosity of the dispersed phase can be adequately approximated by the continuous-phase turbulent viscosity via the Tchen correlation. This approach has been widely validated in helico-axial multiphase pump simulations at comparable operating conditions [5,14]. A mass flow inlet was prescribed at the inlet, and a static pressure outlet of 7 atm was prescribed at the outlet. The interphase momentum transfer was modeled using the Schiller–Naumann drag model, which accounts for the relative motion between the dispersed gas bubbles and the continuous liquid phase. Non-drag forces, including turbulent dispersion and virtual mass, were also included to capture the transient gas–liquid interaction during speed variation. For the comparison between IGVF = 10% and 20%, the total inlet mass flow rate was kept constant, and the IGVF was defined as the ratio of the gas-phase volume flow rate to the total mixture volume flow rate at the inlet (IGVF = Qgas/Qmixture × 100%). The desired IGVF values were achieved by adjusting the individual inlet mass flow rates of the gas and liquid phases while maintaining the same total mass flow rate at the inlet.

The Transient Rotor–Stator model was used at rotor–stator interfaces, with data transferred using the Specified Pitch Angle model. A single-passage computational domain was employed for both the impeller (3 blades) and diffuser (11 blades), with a pitch ratio of 3/11 specified at the rotor–stator interface to account for the unequal blade counts. The rotational speed of the impeller was prescribed according to Equation (1): the impeller rotated counterclockwise when viewed along the flow direction, while all other components were stationary. All walls were specified as smooth, no-slip walls, and automatic wall treatment was used in near-wall regions where turbulence was not fully developed. Root-mean-square residuals were used as the convergence criterion, with a tolerance of 10^{-5}. All numerical simulations were performed using ANSYS CFX 2022 R2 (ANSYS Inc., Pittsburgh, PA, USA). The transient simulations employed a physical time step of 1.0×10^{-4} s, corresponding to approximately 1.8° of impeller rotation per time step at the rated speed of 3000 r/min. A maximum of 10 coefficient loop iterations was allowed per time step, and the RMS residual target of 10^{-5} was consistently achieved within 5–8 iterations. Prior to the transient speed variation stage, the flow field was initialized by running 20 complete revolutions at the rated speed (3000 r/min) under steady-state conditions to ensure a fully developed flow field. A time-step independence study was conducted by comparing results obtained with time steps of 2.0×10^{-4} s, 1.0×10^{-4} s, and 5.0×10^{-5} s. The differences in head, efficiency, and pressure distribution between the 1.0×10^{-4} s and 5.0×10^{-5} s cases were all below 2%, confirming that the 1.0×10^{-4} s time step provides adequate temporal resolution. It should be noted that cavitation effects were not considered in the present simulations. Although local low-pressure regions may occur during transient acceleration, the minimum static pressure in the computational domain remained above the vapor pressure of water at 25 °C (3.17 kPa) for all investigated conditions, as the outlet pressure was maintained at 7 atm. Therefore, cavitation inception is not expected under the present operating conditions, and neglecting cavitation is justified.

4. Experimental Investigation of the Multiphase Pump

4.1. Experimental System

Figure 4 shows the physical model of the pressure-boosting unit of the multiphase pump. The impeller, which is the primary energy transfer component, was manufactured from stainless steel and had a 1.0 mm clearance between the blade tips and the outer casing. Figure 5 shows the in-house multiphase-pump test system and high-speed imaging apparatus. The facility comprised four subsystems: gas supply, liquid supply, gas–liquid mixing, and the pump test rig.

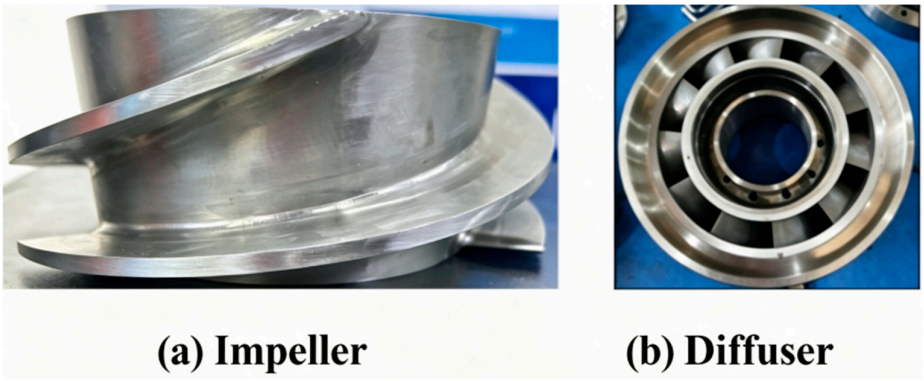


Figure 4. Physical model of the boosting unit of the blade multiphase pump.

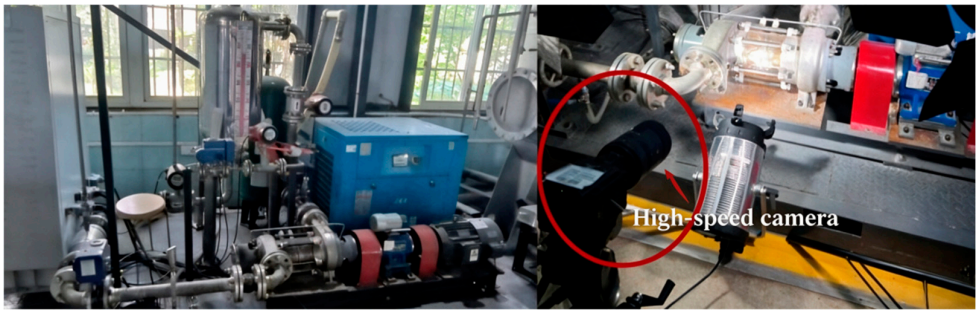


Figure 5. Test system (**left**) and high-speed camera (**right**).

A FASTCAM Mini AX100 high–speed camera (Photron Limited, Tokyo, Japan) was used to capture the complex flow patterns within the impeller passages. For experimental safety and economy, water and air were used as the liquid and gas phases, respectively. During each test, air and water were thoroughly mixed in the piping system and delivered to the pressure-boosting unit. After stable operation was established, the operating condition was varied by adjusting the gas inlet valve opening or the outlet valve opening, while operating parameters and flow pattern images were recorded in real time.

4.2. Numerical and Experimental Validation

To verify the reliability of the numerical model, the external characteristics of a four-stage multiphase pump were tested under pure-water steady-state conditions at 2980 r/min. The experimental measurements and simulated results were compiled and plotted for comparison in Figure 6. The deviation between numerical and experimental results was quantified as $\delta = | (Xnum - Xexp)/Xexp | \times 100\%$, where X denotes head, efficiency, or shaft power. The maximum deviations in head, efficiency, and power were 4.2%, 3.8%, and 4.5%, respectively, all within 5%. Experimental uncertainty bars are provided in Figure 6, indicating that the numerical method provides a reasonable representation of the pump's steady-state single-phase external characteristics. However, direct validation of the transient two-phase results remains a limitation, as discussed below. It should

be acknowledged that the validation was performed under steady-state, single-phase (pure-water) conditions on a four-stage pump geometry, whereas the transient simulations investigated two-phase flow at IGVFs of 10% and 20% on a single-stage model under variable-speed operation. The validation therefore confirms the reliability of the numerical approach for predicting the pump's external characteristics under baseline conditions; direct experimental validation of the transient two-phase results remains a limitation and is recommended for future work. Nevertheless, the employed Eulerian–Eulerian framework with the SST k-ω turbulence model and Schiller–Naumann drag model has been extensively validated in the literature for gas–liquid two-phase flow in multiphase pumps under similar operating ranges [5,14,15].

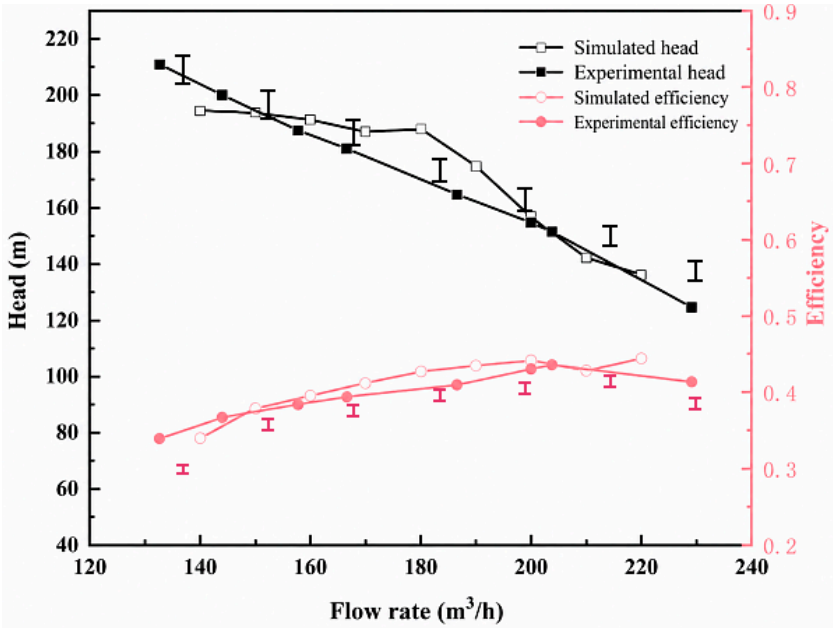


Figure 6. External characteristic curve of the blade multiphase pump. Error bars represent the experimental measurement uncertainty (±2.5% for head, ±2.0% for efficiency, and ±3.0% for power).

5. Variation in External Characteristics

Since the two IGVF cases were compared at a constant total inlet mass flow rate, varying the IGVF also changes the mixture volumetric flow rate. The differences reported below should therefore be interpreted as the effect of changing IGVF under the present constant-total-mass-flow operating condition rather than as a strictly isolated IGVF effect. Figure 7 shows the effects of IGVF on the external characteristics of the multiphase pump under variable-speed conditions. At a given IGVF, the pressure-boosting performance first increased and then decreased as the rotational speed varied. This behavior indicates that the pump's energy transfer capability increases during acceleration and decreases rapidly during deceleration. At the investigated IGVFs of 10% and 20%, increasing the gas fraction reduced the pressure-boosting performance because the larger gas-phase volume fraction lowered the mixture density and weakened energy transfer from the impeller. During acceleration, the increase in hydraulic efficiency at the lower IGVF was greater than that at the higher IGVF. Once deceleration began, the influence of IGVF on hydraulic efficiency was not significant.

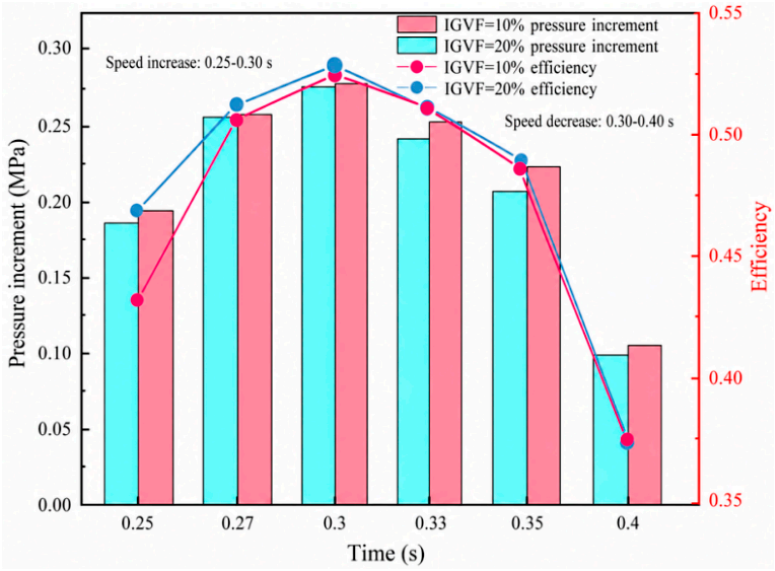


Figure 7. Effects of gas volume fraction on external characteristics of multiphase pump under variable–speed conditions.

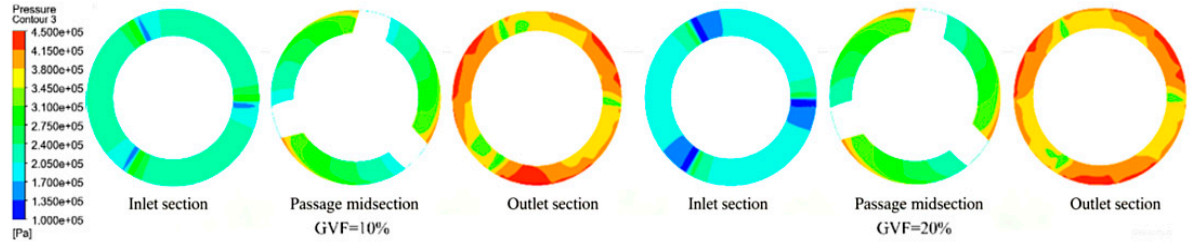
Effects of Variable-Speed Operation on Pressure Distribution Within the Impeller

Because rapid changes in rotational speed markedly affect the external characteristics, the internal flow states at three representative sections (the inlet, passage midsection, and outlet) were examined at six instants to determine the effects of rotational speed and IGVF on the impeller flow field.

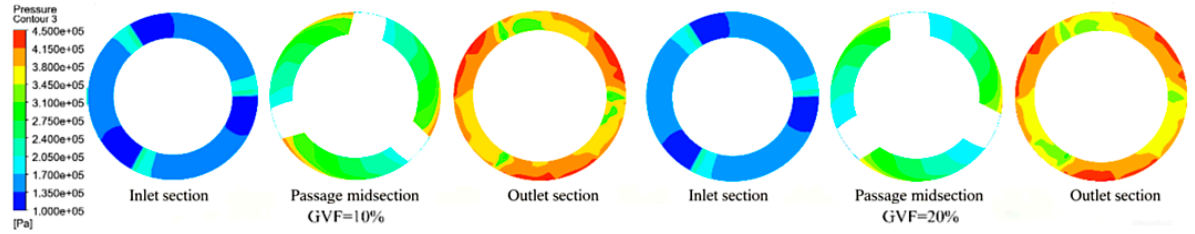
Figure 8 shows pressure contours at the three representative sections for different IGVFs. At 0.25 s, before the rotational speed began to change, the impeller flow was stable. At this instant, the pressure at every section was higher for GVF = 10% than for GVF = 20%. Because centrifugal effects drive the lower-density gas phase toward the hub and the blade suction side, pressure decreased from shroud to hub at each section. Pressure also increased from inlet to outlet; consequently, the maximum pressure within the impeller occurred near the outlet shroud.

The evolution of the sectional pressure contours can be interpreted in terms of rotational-speed variation. During acceleration (0.25–0.30 s), the low-pressure region at the inlet section contracted as rotational speed increased. At first sight, this behavior appears inconsistent with the expectation that a higher impeller speed increases the work input to the fluid and therefore raises pressure throughout the flow field. The discrepancy arises from fluid inertia: fluid velocity cannot change instantaneously. Thus, although the impeller speed was increasing at 0.27 and 0.30 s, the inlet static pressure remained lower than its steady-state value at 0.25 s. In contrast, pressure increased at the passage midsection and outlet because fluid already present within the impeller received additional energy from the accelerating blades. The resulting increase in flow energy density appeared as an increase in static pressure, most prominently at the outlet section where energy accumulated. During deceleration (0.30–0.40 s), this process was reversed. As rotational speed decreased, energy input by the impeller declined, pressure decreased at all sections, high-pressure regions progressively contracted, and the pressure gradient through the passage became weaker, clearly reflecting the reduction in energy input. IGVF also exerted a pronounced influence on pressure distribution. At every section and throughout the speed change process, impeller pressure at GVF = 20% was substantially lower than that at GVF = 10%. The transient nature of gas–liquid two-phase flow was particularly evident under variable-speed conditions. At the higher GVF of 20%, the spatial pressure distribution changed more rapidly with time; for example, the low-pressure region at

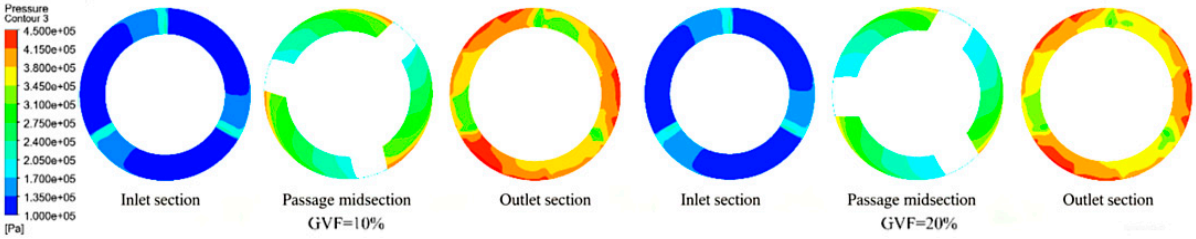
the inlet disappeared more quickly. This result indicates that, at the investigated IGVFs, a higher gas fraction increases the transient response sensitivity of the pressure field to rotational-speed changes.



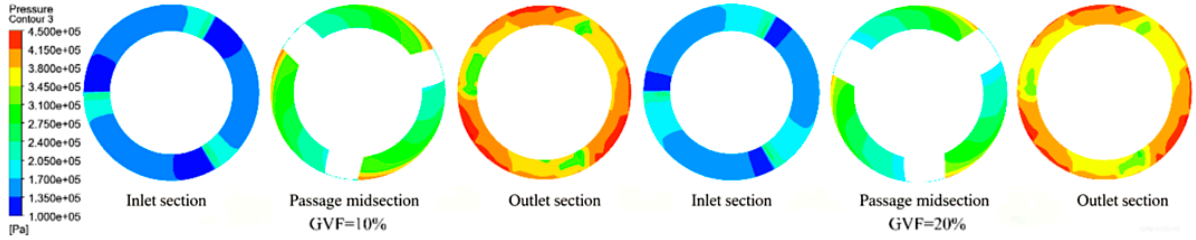
(**a**) Pressure nephograms of different sections under varied inlet gas contents, t = 0.25 s.



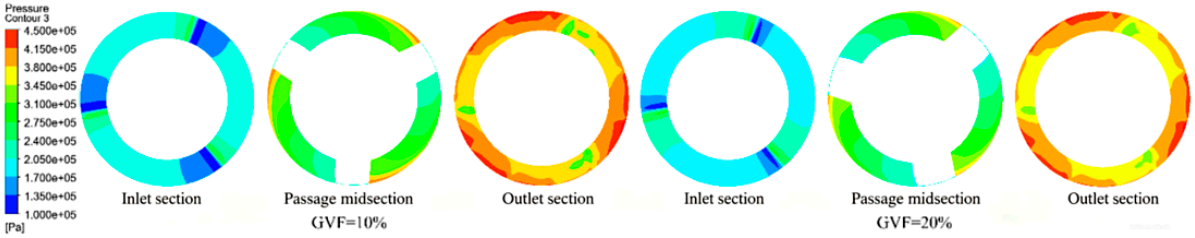
(**b**) Pressure nephograms of different sections under varied inlet gas contents, t = 0.27 s.



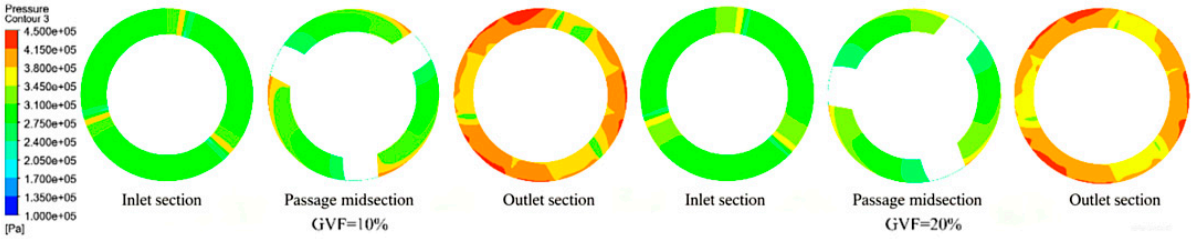
(**c**) Pressure nephograms of different sections under varied inlet gas contents, t = 0.30 s.



(**d**) Pressure nephograms of different sections under varied inlet gas contents, t = 0.33 s.



(**e**) Pressure nephograms of different sections under varied inlet gas contents, t = 0.35 s.



(**f**) Pressure nephograms of different sections under varied inlet gas contents, t = 0.40 s.

Figure 8. Pressure distribution nephograms of three characteristic sections inside the impeller under different inlet gas content conditions.

During variable-speed operation, the internal flow state of the multiphase pump is governed by the coupling between the dynamic effects induced by rotational-speed variation and interphase interactions in the gas–liquid two-phase flow.

All panels within each IGVF condition share the same pressure color scale, ranging from approximately 0.10 MPa to 0.45 MPa, to facilitate direct visual comparison across the three sections and six time instants.

6. Effects of Variable-Speed Operation on Impeller Work Performance

6.1. Effects of Variable-Speed Operation on Blade Loading Distribution

Figure 9 shows the blade pressure load distributions at GVF = 20% under variable-speed conditions. Figure 9 presents the static pressure distributions on both the pressure side and suction side of the blade at each streamwise location; blade loading is represented by the difference between these two curves. Comparison of Figures 1 and 9 shows that, at different rotational speeds, the pressure load distributions on the pressure and suction sides follow similar streamwise trends from inlet to outlet. The instant 0.25 s represents the initial speed and steady operation. During acceleration (0.25–0.30 s), overall blade loading at 0.27 s was lower than that at 0.25 s, but increased again at 0.30 s. This behavior indicates that an abrupt speed change temporarily disrupts the flow and impairs impeller work. Increasing rotational speed also increased the load peak and the abrupt load variation at the inlet while shifting the equal-load point toward the outlet. Thus, acceleration enhances impeller work but also intensifies inlet incidence caused by flow instability. During deceleration, both the load peak and the abrupt inlet variation decreased, the equal-load point moved away from the inlet, and the impeller's energy transfer capability declined with rotational speed.

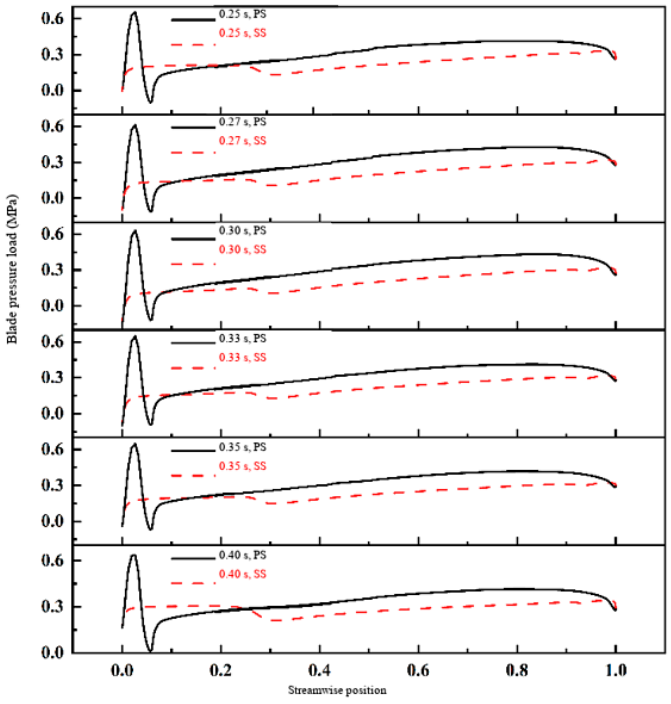


Figure 9. Pressure load distribution curve of impeller blades under variable–speed condition (GVF = 20%).

Figure 9 also shows that, at a given rotational speed, the pressure load on both the pressure and suction sides first increases and then decreases from inlet to outlet. An abrupt load variation occurs on the pressure side near the inlet because backflow, vortices, rotor–stator interaction, and incidence cause local fluctuations in blade surface pressure.

The ordinate represents the static pressure on the blade pressure side (PS) and suction side (SS), and the abscissa is the streamwise position normalized by the blade chord length.

Figure 10 shows the effects of IGVF on blade loading distributions under variable-speed conditions. Under every operating condition, the pressure-side curve exhibits a peak near the inlet, then rises gradually in the streamwise direction before decreasing near the outlet. The inlet peak indicates the presence of backflow and inflow incidence. The suction-side curve generally increases from inlet to outlet but contains several inflection points and local minima in the middle of the passage, indicating that the suction-side flow is more strongly disturbed by gas–liquid phase distribution and vortex shedding and is therefore substantially less stable than the pressure-side flow. As rotational speed increases, the enclosed area formed by the intersections of the pressure- and suction-side curves expands, demonstrating increased energy transfer from the impeller to the fluid; this area contracts as the speed decreases. During acceleration, the load curves at the two IGVFs increasingly overlap. A higher speed increases interphase shear and turbulent kinetic energy, promotes more uniform gas–liquid mixing, and rapidly raises pressure. Compression of the gas phase reduces its volume fraction and weakens the difference between the two inlet conditions. During deceleration, IGVF has a progressively greater influence on blade loading, and the two sets of load curves separate more clearly. At a given rotational speed, the enclosed region for GVF = 20% lies farther downstream than that for GVF = 10%, indicating that increasing IGVF is detrimental to impeller work. IGVF affects the pressure and suction sides differently. At GVF = 20%, the pressure-side load is consistently higher than at GVF = 10%, suggesting that the gas–liquid mixture produces stronger incidence on the pressure side. The suction side does not follow the same trend because gas preferentially accumulates there and vortices readily form under the pressure gradient.

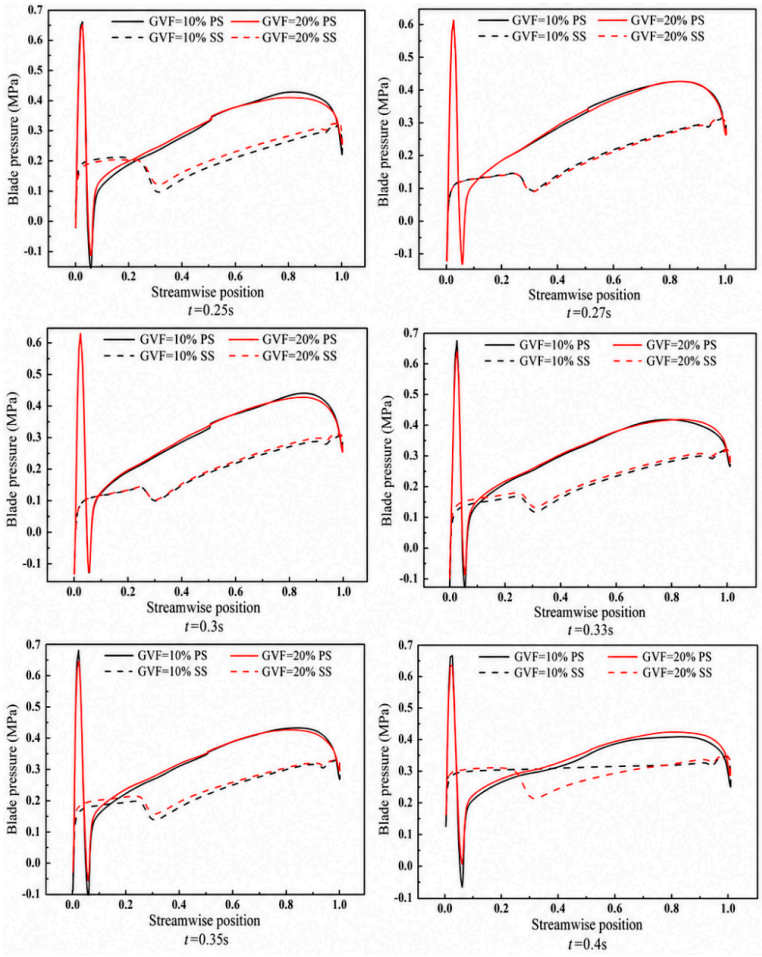


Figure 10. Effects of different inlet gas contents on load distribution of multiphase pump blades under variable−speed conditions.

Analysis of the effects of IGVF on blade loading under variable-speed conditions shows that, at high rotational speeds, the pump is relatively insensitive to IGVF variation and can maintain stable operation. At low rotational speeds, however, the influence of IGVF is amplified and flow stability deteriorates.

The curves represent the static pressure on the blade pressure side (PS) and suction side (SS), and the streamwise coordinate is normalized by the blade chord length.

6.2. Effects of Variable-Speed Operation on Dynamic and Static Head Within the Impeller

According to the Bernoulli energy equation:

$$H_{T\infty} = \frac{(P_2 - P_1)}{\rho g} + \frac{(V_2^2 - V_1^2)}{2g} + (z_2 - z_1) \tag{4}$$

where P_1 and P_2 are the static pressures at the impeller inlet and outlet, respectively, in Pa; V_1 and V_2 are the absolute velocities at the impeller inlet and outlet, respectively, in m/s; and z_1 and z_2 are the elevation heads at the impeller inlet and outlet, respectively. Because the elevation difference between the inlet and outlet of the multiphase pump is small, the potential head difference is neglected.

Equation (4) indicates that the energy acquired by the fluid from the impeller consists primarily of static head, dynamic head, and potential head. However, it does not describe the relationship between the energy and velocity of each phase during energy transfer in a multiphase pump. An alternative form of the Euler equation can therefore be written as follows:

$$H_{T\infty} = \frac{(v_2^2 - v_1^2)}{2g} + \frac{(w_1^2 - w_2^2)}{2g} + \frac{(u_2^2 - u_1^2)}{2g} \tag{5}$$

where the left-hand side denotes the theoretical head; u, v, and w are the peripheral, absolute, and relative velocities, respectively; and subscripts 1 and 2 denote the impeller inlet and outlet. The first term represents the kinetic energy change caused by the variation in absolute velocity and corresponds to the dynamic head. The second term represents conversion of velocity head into pressure head as the relative velocity changes within the impeller, thereby producing static head; this is referred to as the blade-lift work term. The third term represents the increase in static head caused by centrifugal effects and is referred to as the centrifugal force term. Thus, the first term $(\Delta(v^2)/2g)$ corresponds to the dynamic head, whereas the sum of the second and third terms corresponds to the static head produced by the impeller.

Figure 11 shows the streamwise variations in dynamic and static head within the impeller at different rotational speeds. The streamwise coordinate is normalized by the impeller blade chord length, with a value of 1.0 corresponding to the blade leading edge and 2.0 corresponding to the trailing edge. At each streamwise location, the dynamic and static heads are defined relative to their corresponding values at the impeller inlet. The distributions at 0.25 and 0.35 s are similar because the rotational speeds at these two instants are the same. The largest dynamic and static heads occurred at 0.27, 0.30, and 0.33 s, corresponding to the highest rotational speeds, whereas the lowest values occurred at 0.40 s, when the rotational speed was lowest. Nevertheless, the head magnitudes at 0.27, 0.30, and 0.33 s did not directly follow the instantaneous rotational speed because the internal flow field responds with a delay owing to fluid inertia. Comparison of the two IGVFs shows that the maximum dynamic and static heads occurred at 0.30 s for GVF = 20%, but at 0.33 s for GVF = 10%. The higher gas fraction reduces the mixture density and therefore weakens inertial effects. The static head at GVF = 20% was generally lower than that at GVF = 10%, demonstrating that increasing IGVF reduces static head production and weakens the impeller's energy transfer capability. In the streamwise distribution, the

static head remained close to zero near the inlet, where the fluid had not yet received substantial work. In the middle region (0.2–0.8 of the normalized chord length), the static head increased continuously while the dynamic head became progressively more negative, identifying this region as the principal work input zone. Near the outlet, both dynamic and static head decreased, indicating insufficient recovery of kinetic energy and impaired conversion to pressure energy because of rotor–stator interaction.

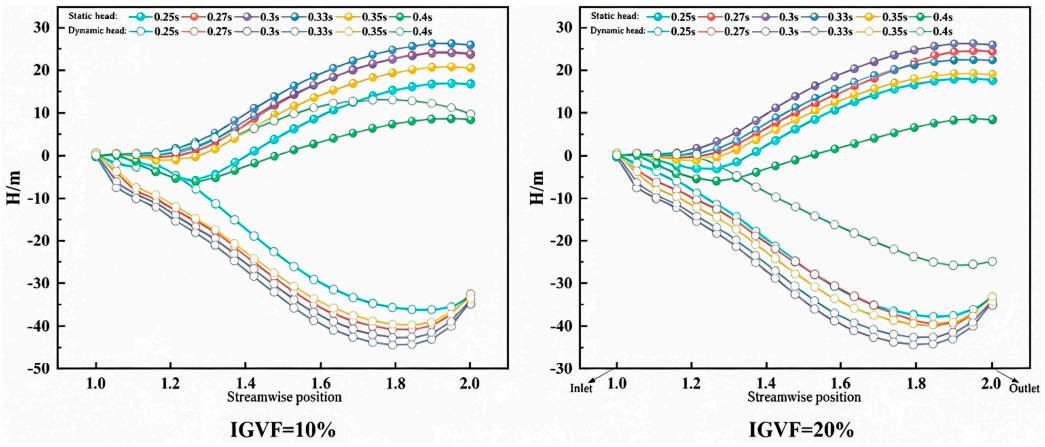


Figure 11. Effects of variation law of dynamic and static head in impeller under different rotating speeds.The streamwise coordinate is normalized by the blade chord length (1.0 = leading edge, 2.0 = trailing edge).

6.3. Effects of Variable-Speed Operation on Power Within the Impeller

To further characterize energy conversion in the multiphase pump, the energy acquired by the fluid at ten sections within the impeller—the principal work input component—was analyzed, as illustrated in Figure 12. The ten sections are evenly distributed along the impeller axial direction, with Section 1 located at the blade leading edge (inlet) and Section 10 located at the blade trailing edge (outlet). Each section is separated by approximately one-tenth of the blade axial chord length. Because hydraulic losses prevent all energy transferred by the impeller from being converted into useful energy, the energy acquired by the fluid across the axial flow sections was evaluated using the following formulation:

$$P_a = \int_A pavndA = \int_A (p_s + p_d)vndA = \int_A p_s vndA + \int_A p_d vndA = P_s + P_d \quad (6)$$

where P_a is the total pressure power; P_s and P_d are the static and dynamic pressure power, respectively; p_s, p_d, and pa are the static, dynamic, and total pressures in the absolute reference frame, respectively; v is the velocity obtained from the conservation equations; and n is the unit normal vector.

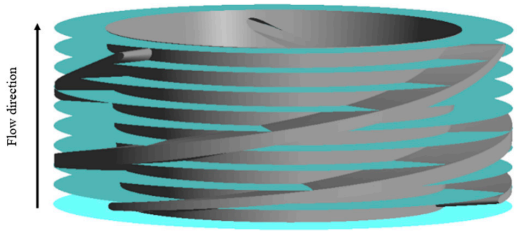


Figure 12. Section division of multiphase pump 1–10.

It should be noted that in the present two-phase simulations, the velocities and densities employed in Equations (5) and (6) refer to the volume-weighted mixture density and the mass-averaged mixture velocity at each section, rather than phase-resolved values.

Because the Eulerian–Eulerian framework permits interphase slip and accounts for gas compressibility through the ideal gas law, a strict phase-resolved energy balance would require separate treatment of each phase's pressure and velocity fields. Accordingly, the decomposition into static pressure and dynamic pressure power presented here should be interpreted as an engineering diagnostic tool for assessing the relative contributions of pressure work and kinetic energy change along the impeller, rather than as a rigorous phase-resolved energy balance. This diagnostic approach is commonly adopted in multiphase pump analysis and is sufficient for identifying the dominant energy conversion mechanisms and their trends under variable-speed operation.

Figure 13 shows the distributions of power at impeller Sections 1–10 for different rotational speeds. In the streamwise direction, from Section 1 to Section 10, the energy input from the impeller to the fluid increased progressively. As the fluid traveled axially through the impeller, it continuously received mechanical energy from the blades. This energy accumulated in the flow direction, causing the total power to increase overall from Section 1 to Section 10. Changing IGVF had only a limited effect on total power, consistent with the external characteristic results, but altered the relative contributions of dynamic and static pressure power. At the same section and instant, increasing IGVF reduced the total power, confirming that a higher gas fraction suppresses energy conversion in the impeller. Rotational speed also affected power differently at different streamwise positions. Closer to the impeller inlet, static pressure power was more sensitive to speed variation. Static pressure power dominated near the inlet and initially decreased as the rotational speed increased. When the speed rose abruptly from its steady value, the flow entering the first several sections could not immediately adapt to the change, intensifying gas–liquid interaction and increasing hydraulic loss. Static pressure power subsequently increased during deceleration because fluid inertia allowed the impeller to continue transferring energy even as the speed decreased. In the middle and rear work input regions, dynamic and static pressure power responded differently to speed variation. During acceleration (0.25–0.30 s), dynamic pressure power increased because the circumferential fluid velocity rose with impeller peripheral speed. Static pressure power also increased continuously owing to enhanced static pressure work by the blades and consistently accounted for more than 50% of total power, indicating that the energy acquired by the fluid was dominated by static pressure energy. During deceleration (0.30–0.40 s), the impeller's energy transfer capability weakened with decreasing speed, and both dynamic and static pressure power declined. The direct power response in this stage indicates that rotational speed governs the impeller's energy transfer capability.

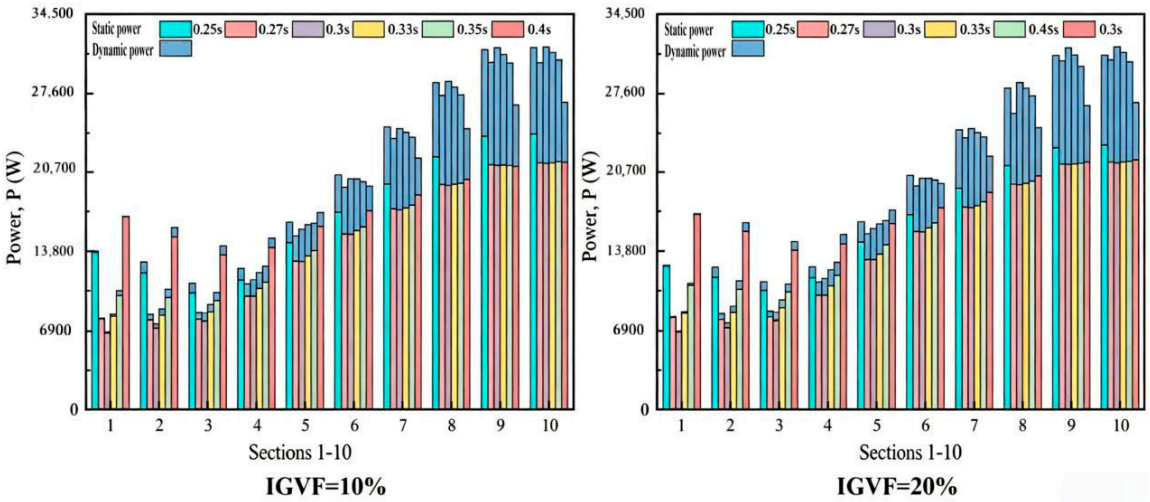


Figure 13. Distribution of power variation of impeller sections 1–10 under different rotating speeds.

Sections 1–10 are evenly distributed along the impeller axial direction from the blade leading edge (Section 1) to the trailing edge (Section 10).

7. Conclusions

(1) The energy transfer capability of the multiphase pump increased with rotational speed and decreased rapidly during deceleration. During acceleration (0.25–0.30 s), the hydraulic efficiency increased more markedly at the lower IGVF than at the higher IGVF, as shown in Figure 7; During acceleration, the increase in hydraulic efficiency at the lower IGVF was greater than that at the higher IGVF. Once deceleration began, the effect of IGVF on hydraulic efficiency was not significant (variation below 0.5 percentage points).

(2) At the investigated IGVFs of 10% and 20%, a higher gas fraction was associated with a more pronounced transient response of the internal pressure field to speed variation. Specifically, during acceleration, the spatial pressure distribution at the impeller inlet evolved more rapidly at IGVF = 20% than at IGVF = 10%, and the low-pressure region at the inlet contracted and disappeared more quickly at the higher IGVF, indicating greater transient sensitivity of the flow field to speed changes. An abrupt change in rotational speed disrupted the flow and temporarily impaired impeller work. Acceleration enhanced the impeller's energy transfer capability but also intensified inlet incidence caused by flow instability. During deceleration, both the peak load and the abrupt load variation near the inlet decreased, the equal-load point moved away from the inlet, and the energy transfer capability declined with rotational speed.

(3) Increasing IGVF suppressed energy conversion in the impeller, primarily by reducing static head production through the combined effects of diminished blade-lift work and weakened centrifugal pressurization. Rotational speed affected power differently at different streamwise positions, and static pressure power was more sensitive to speed variation near the impeller inlet. During acceleration, dynamic pressure power increased as circumferential fluid velocity rose with impeller peripheral speed, while static pressure power also increased continuously owing to enhanced static pressure work by the blades; static pressure power consistently accounted for more than half of the total power across all investigated conditions, indicating that the energy acquired by the fluid was dominated by static pressure energy. During deceleration, the impeller's energy transfer capability weakened with decreasing speed, and both dynamic and static pressure power declined. It should be noted that these conclusions are based on simulations at IGVFs of 10% and 20%; extension to higher gas fractions (GVF $\geq$ 50%), where gas accumulation may induce flow asymmetry and abrupt head degradation, requires further investigation.

(4) The present study is subject to several limitations that should be acknowledged. First, the numerical model was validated only under steady-state, single-phase (pure-water) conditions; direct experimental validation of the transient two-phase results under variable-speed operation remains to be performed. Second, only two IGVF conditions (10% and 20%) were investigated, and the findings may not be directly extrapolated to higher gas fractions where flow patterns and energy conversion mechanisms may differ qualitatively. Third, the Dispersed Phase Zero Equation turbulence model for the gas phase, while adequate for the moderate IGVFs and small bubble diameters considered here, may become less accurate at higher gas loadings where bubble coalescence and breakup become significant. Future work should include (i) transient two-phase experimental validation using high-speed photography and dynamic pressure measurements under variable-speed conditions, (ii) extension to a broader range of IGVFs (e.g., 5–50%) to establish general trends, and (iii) comparison with more advanced Eulerian–Eulerian or Eulerian–Lagrangian approaches to assess the sensitivity of the results to the turbulence and interphase force models.

Author Contributions: Conceptualization, R.G. and G.S.; methodology, R.G.; software, Z.C.; validation, Q.P. and T.F.; investigation, A.D.; data curation, A.D.; writing—original draft preparation, R.G. and G.S.; writing—review and editing, A.D.; project administration, Z.C.; funding acquisition, Q.P. All authors have read and agreed to the published version of the manuscript.

Funding: This research was funded by the Outstanding Youth Science Foundation of the Sichuan Provincial Natural Science Foundation (Grant No. 2024NSFJQ0012), the Key Project of the Regional Innovation and Development Joint Fund of the National Natural Science Foundation of China (Grant No. U23A20669), and the National Natural Science Foundation of China (Grant No. 52576038).

Data Availability Statement: The original contributions presented in this study are included in the article. Further inquiries can be directed to the corresponding authors.

Conflicts of Interest: Rui Guo, Guangtai Shi, Zhongbin Chen, Qingxi Pei, and Tongde Feng are employed by Changqing Oilfield No. 7 Oil Production Plant. The remaining authors declare that the research was conducted in the absence of any commercial or financial relationships that could be construed as a potential conflict of interest. The authors declare that this employment did not influence the design of the study, data collection, analysis, interpretation of results, writing of the manuscript, or the decision to submit the manuscript for publication. No other conflicts of interest are declared.

References

1. Murakami, M.; Minemura, K. Effects of entrained air on the performance of a centrifugal pump: 1st report, performance and flow conditions. *Bull. JSME* **1974**, *17*, 1047–1055. [CrossRef]
2. Murakami, M.; Minemura, K. Effects of entrained air on the performance of centrifugal pumps: 2nd report, effects of number of blades. *Bull. JSME* **1974**, *17*, 1286–1295. [CrossRef]
3. Zhang, J.Y.; Cai, S.J.; Zhu, H.W.; Qiang, R. Visualization of gas-liquid two-phase flow patterns in a helico-axial pump. *J. Eng. Thermophys.* **2015**, *36*, 1937–1941.
4. Yu, Z.Y.; Liu, Y. Unsteady gas-liquid two-phase flow characteristics in a multiphase pump. *Trans. Chin. Soc. Agric. Mach.* **2013**, *44*, 1937–1941.
5. Deng, Y.; Li, Y.; Xu, J.; Kuang, C.; Zhang, Y. The influence of blade tip clearance on the flow field characteristics of the gas–liquid multiphase pump. *Processes* **2023**, *11*, 3170. [CrossRef]
6. Yu, Z.Q.; Wang, J.; Liu, R. Internal-flow and energy characteristics of an axial-flow blood pump at different rotational speeds. *J. Eng. Thermophys.* **2024**, *45*, 3698–3705.
7. Lu, J.; Guo, Y.; Zhou, B.; Zhao, M.; Zhang, C.; Huang, C.; Liu, X. Transient hydraulic characteristics and energy loss mechanisms in a variable-speed pumped storage unit operating in pump mode. *J. Energy Storage* **2026**, *151*, 120313. [CrossRef]
8. Tsukamoto, H.; Ohashi, H. Transient characteristics of a centrifugal pump during startup period. *J. Fluids Eng.* **1982**, *104*, 6–13. [CrossRef]
9. Tan, L.W.; Niu, G.P.; Shi, W.D.; Shi, Z.; Chen, C. Experimental study on pressure pulsations in a centrifugal pump at different rotational speeds. *J. Nantong Univ. (Nat. Sci. Ed.)* **2020**, *19*, 56–63.
10. Yu, A.; Wang, Y.; Tang, Q.; Lv, R.; Yang, Z. Investigation of the vortex evolution and hydraulic excitation in a pump-turbine operating at different conditions. *Renew. Energy* **2021**, *171*, 462–478. [CrossRef]
11. Luo, Y.; Dong, J.; Han, Y.J. Experimental study on transient rotational-speed characteristics of a centrifugal pump under cavitating conditions. *J. Vib. Shock* **2021**, *40*, 23–28.
12. Zuo, Z.; Tan, L.; Shi, W.; Chen, C.; Ye, J.; Francis, E.M. Transient Characteristic Analysis of Variable Frequency Speed Regulation of Axial Flow Pump. *Sustainability* **2022**, *14*, 11143. [CrossRef]
13. Liu, M.; Tan, L.; Cao, S. Influence of viscosity on energy performance and flow field of a multiphase pump. *Renew. Energy* **2020**, *162*, 1151–1160. [CrossRef]
14. Li, C.; Luo, X.; Feng, J.; Zhu, G.; Xue, Y. Effects of gas-volume fractions on the external characteristics and pressure fluctuation of a multistage mixed-transport pump. *Appl. Sci.* **2020**, *10*, 582. [CrossRef]
15. Xu, Y.; Cao, S.; Sano, T.; Wakai, T.; Reclari, M. Experimental investigation on transient pressure characteristics in a helico-axial multiphase pump. *Energies* **2019**, *12*, 461. [CrossRef]
16. Ji, L.; Li, W.; Shi, W.; Chang, H.; Yang, Z. Energy characteristics of mixed-flow pump under different tip clearances based on entropy production analysis. *Energy* **2020**, *199*, 117447. [CrossRef]
17. Liu, J.; Liu, C. Modified normalized Rortex/vortex identification method. *Phys. Fluids* **2019**, *31*, 061704. [CrossRef]

18. Zhang, W.; Shi, L.; Tang, F.; Sun, Z.-Z.; Zhang, Y. Identification and analysis of the inlet vortex of an axial-flow pump. *J. Hydrodyn.* **2022**, *34*, 234–243. [CrossRef]
19. Nayak, A.; Das, D. Experimental and numerical investigation of flow instability in a transient pipe flow. *J. Fluid Mech.* **2021**, *920*, A39. [CrossRef]
20. Wu, Y.; Zhang, W.; Wang, Y.; Zou, Z.; Chen, J. Energy dissipation analysis based on velocity gradient tensor decomposition. *Phys. Fluids* **2020**, *32*, 035114. [CrossRef]
21. Zhang, Y.; Liu, K.; Li, J.; Xian, H.-Z.; Du, X.-Z. Analysis of the vortices in the inner flow of reversible pump turbine with the new omega vortex identification method. *J. Hydrodyn.* **2018**, *30*, 463–469. [CrossRef]
22. Han, L.Y. Evolution of Vortex Structures in a Waterjet Propulsion Pump and the Effects of Cavitation on Vortex Structures. Ph.D. Thesis, Jiangsu University, Jiangsu, China, 2021.
23. Xie, Y.T. Characteristics of Unsteady Vortex Structures and Vortex-Dynamics Diagnosis in a Mixed-Flow Pump. Ph.D. Thesis, Jiangsu University, Jiangsu, China, 2020.
24. Feng, J.; Luo, X.; Guo, P.; Wu, G. Influence of tip clearance on pressure fluctuations in an axial flow pump. *J. Mech. Sci. Technol.* **2016**, *30*, 1603–1610. [CrossRef]

Disclaimer/Publisher's Note: The statements, opinions and data contained in all publications are solely those of the individual author(s) and contributor(s) and not of MDPI and/or the editor(s). MDPI and/or the editor(s) disclaim responsibility for any injury to people or property resulting from any ideas, methods, instructions or products referred to in the content.